Molecular Vision 2020; 26:257-276 <http://www.molvis.org/molvis/v26/257>
Received 24 October 2018 | Accepted 30 March 2020 | Published 1 April 2020

Long-term evaluation of retinal morphology and function in a mouse model of oxygen-induced retinopathy

Olachi J. Mezu-Ndubuisi,[1,2] Erica L. Macke,[3] Raja Kalavacherla,[1] Amy Amanda Nwaba,[4] Andrew Suscha,[2] Ismail S. Zaitoun,[2] Akihiro Ikeda,[3] Nader Sheibani[2,5,6]

[1]Department of Pediatrics, University of Wisconsin School of Medicine and Public Health, Madison, WI; [2]Department of Ophthalmology and Visual Sciences, University of Wisconsin School of Medicine and Public Health, Madison, WI; [3]Department of Medical Genetics, University of Wisconsin-Madison, Madison, WI; [4]Vanderbilt University, Nashville, TN; [5]Department of Biomedical Engineering, University of Wisconsin School of Medicine and Public Health, Madison, WI; [6]Department of Cell and Regenerative Biology, University of Wisconsin School of Medicine and Public Health, Madison, WI

Purpose: Retinopathy of prematurity (ROP) is a condition of aberrant retinal vascularization in premature infants in response to high levels of oxygen used for critical care that can potentially cause blindness. Although therapies to mitigate vascular abnormalities are being evaluated, functional deficits often remain in patients with treated or regressed ROP. This study investigated long-term outcomes of hyperoxia on retinal morphology and function using a mouse model of oxygen-induced ischemic retinopathy (OIR).

Methods: Twenty-two mice were exposed to 77% oxygen to induce OIR, while 23 age-matched control mice were raised in room air (RA). In vivo fluorescein angiography (FA), spectral-domain optical coherence tomography (SD-OCT), and focal electroretinography (fERG) were performed at P19, P24, P32, and P47, followed by histological assessments of retinal morphology, gliosis, microglia activation, and apoptosis.

Results: FA in OIR mice showed capillary attrition despite peripheral revascularization. Inner retina thinning was detected with SD-OCT; outer and inner retinal dysfunction were demonstrated with fERG. Histology of the OIR mice exhibited a thin, disorganized structure. Immunohistochemistry showed increased gliosis, microglial activation, and apoptosis with increasing age from P19 to P47. The synapses between rod photoreceptor cells and rod bipolar cells were ectopically localized in the OIR mice.

Conclusions: We demonstrated histological evidence of persistent ectopic synapses, prolonged cellular apoptosis, and gliosis in the OIR retina that corresponded with long-term in vivo evidence of capillary attrition, inner retinal thinning, and dysfunction despite full peripheral revascularization. Further studies on the mechanisms underlying these persistent phenotypes could enhance our understanding of ROP pathogenesis and lead to new therapeutic targets to preserve visual function in premature infants.

Retinopathy of prematurity (ROP) is a disorder of retinal vascular development primarily affecting premature infants exposed to high levels of supplemental oxygen. Hyperoxia causes downregulation of vascular endothelial growth factor (VEGF), a cytokine critical for angiogenesis, which leads to arrested growth of immature developing retinal vessels [1,2]. As the infant matures, the retina becomes hypoxic due to the inadequate vascular supply, triggering abnormal excessive upregulation of VEGF, which leads to pathologic neovascularization [2]. Despite current treatments for ROP, such as laser therapy to ablate the avascular retina [3] and intravitreal anti-VEGF therapy [4], ROP continues to be the leading cause of childhood blindness in the world [5,6]. Infants treated for ROP, either with laser or anti-VEGF therapy [7,8], and premature infants with untreated mild ROP which has regressed [9,10], are at increased risk for adverse long-term visual sequela at school age, such as refractive error, strabismus, glaucoma, and visual impairment, compared to full-term infants. This suggests the existence of an abnormality early in the process of retinal development of premature infants. Therefore, enhanced understanding of the long-term effects of oxidative stress on the developing retinal structure beyond retinal vascularization would be important in discovering more effective treatment alternatives to preserve long-term visual function.

Retinal vascularization develops concurrently with the maturation of the retinal neuronal cells and glia cells [11]. Retinal glia cells (microglia and macroglia) provide a supporting network for retinal neurons [11], serve as a scaffolding guide to developing retinal vessels [12], and survey the retina for potential injury or infection to provide protection of the neuronal milieu [13,14]. Upon oxidative injury, the retinal glial cells are activated [15]. Reactive glial cells can either support neuronal cell survival or accelerate neuronal degeneration and dysfunction [11].

Correspondence to: Olachi J. Mezu-Ndubuisi, 600 Highland Avenue, H4-431, Madison, WI 53792; Phone: (608) 265 0853; FAX: (608) 265 3397; email: olachimezu@pediatrics.wisc.edu

Retinal macroglia, made up of astrocytes and Müller cells, are activated in mice with oxygen-induced retinopathy (OIR) in a process known as gliosis [16,17]; microglia activation has been described in OIR mice as correlating with retinal neovascularization [15,16]. Müller cell gliosis and microglial activation have been shown to correlate with the absence of the deep vascular plexus or avascularity in the retinas of OIR mice [16]. However, the time course and duration of microglia activation and gliosis with respect to retinal vascularization in the OIR phenotype are relatively unknown.

Murine models of oxygen-induced ischemic retinopathy have been used to mimic vascular [18,19] and structural [20] abnormalities in human ROP using histological techniques, but are limited in physiologic studies. In previous studies, we used in vivo retinal imaging to study retinal vascularization, structure, and function [21] in live OIR mice. The in vivo OIR phenotype demonstrated persistent capillary regression, inner retinal thinning, and abnormal neuronal function in adult OIR mice despite full peripheral retinal vascularization. In the present study, our objective was to use histological and in vivo techniques to study the time course of the ROP phenotypes in OIR mice, specifically the retinal glial cells, cellular apoptosis, and neuronal synaptic integrity. This would provide insights into studies of mechanistic pathways regulating retinal cells, neurons, and blood vessels, and be critical to identifying new therapies to fully rescue the ROP phenotype and prevent long-term visual deficits in preterm infants.

METHODS

Animals: Wild-type C57BL/6J mice (Jackson Laboratory, Bar Harbor, ME) were reared under approved protocols by the Institutional Animal Care and Use Committee of the University of Wisconsin School of Medicine and Public Health, and in compliance with the Association for Research in Vision and Ophthalmology Statement for the Use of Animals in Ophthalmic and Vision Research. At postnatal day (P) 7, 22 mice were exposed to 77 ± 2.0% oxygen in a chamber (Biospherix ProOX 110; Apex Laboratory, Redwing, MN) with nursing dams for 5 days, while 23 mice were raised in room air (RA), as previously described in a published modification [22], of an established mouse OIR protocol [18]. In vivo and histological studies were performed at P19, P24, P32, and P47, representing each phase of retinal vascular development, early (P16–P20), mid (P23–P27), late (P30–P34), and mature (beyond P35), as previously published. All applicable international, national, and/or institutional ethical guidelines for the care and use of animals were met.

In vivo studies: Fluorescein angiography (FA), spectral domain-optical coherence tomography (SD-OCT), and focal electroretinogram (fERG) studies were performed in live, anesthetized mice using a retinal imaging system, Micron IV (Phoenix Research Laboratories, Pleasanton, CA), according to the manufacturer's instructions. FA, SD-OCT, and fERG were performed at P19, P24, P32, and P47.

Focal electroretinograms: To study the function of retinal neurons, fERG was recorded in the OIR and RA mice at P19, P24, P32, and P47. After 4 h of dark adaptation, intraperitoneal (IP) ketamine (100 mg/kg) and xylazine (10 mg/kg) were used for mice anesthesia. The eyes were dilated before fERG using the manufacturer's laboratory scribe software. A circular region of interest (ROI) was positioned 2 disc diameters from the optic nerve between two major retinal vessels, as previously described. Flash stimuli lasting 6 ms at varying flash intensities were triggered to generate increasing energy of 0.1 log cd.sec/m^2, 0.3 log cd.sec/m^2, 1.0 log cd.sec/m^2, and 3.0 log cd.sec/m^2. Ten recordings were averaged with 20 s recovery time between the flash intensities. Amplitudes and peak times for a-waves and b-waves were automatically calculated. The a-wave is the total amplitude measured from the beginning of the recording to the lowest point or trough of the negative deflection. The b-wave amplitude is measured from the lowest deflection or trough of the a-wave to the highest point or peak of the b-wave. The peak times represent the time in milliseconds from the light flash initiation to the trough of the a-wave (a-wave peak time) and the peak of the b-wave (b-wave peak time).

FA and SD-OCT: Following fERG, while the animals were anesthetized and eyes dilated, simultaneous FA and SD-OCT were performed. Ten percent sodium fluorescein (100 mg/kg; AK-FLUOR, Akorn, Decatur, IL) was administered intraperitoneally. Then, circular FA images were obtained in each mouse, as previously described [22]. In the same ROI where fERG was performed, a circle SD-OCT scan pattern was placed within 2 disc diameters of the optic nerve head, and SD-OCT scans were obtained as previously published [23]. The total, outer, and inner retinal area thicknesses were automatically generated, along with a retinal thickness color map. The retinal avascular area (RAA) was quantified as a percentage (%) of the total retinal area using a customized MATLAB software program, as previously published.

Histological studies: Following the in vivo studies, the same mice were used for the histological studies. The mice were asphyxiated using CO_2, and both eyes were enucleated and fixed at 4 °C. All histological studies were performed at P19, P24, P32, and P47.

Analysis of thickness of retinal cross sections: Right eyes were immersion fixed in Bouin's fixative overnight at 4 °C, then rinsed, dehydrated, and embedded in paraffin. Paraffin blocks were sectioned 6 µm thick on an RM2135 microtome (Leica Microsystems, Wetzlar, Germany) and mounted on glass slides. The slides were then stained with hematoxylin and eosin (H&E) to visualize the retinal structure. H&E-stained sections were imaged on an Axio Scope.A1 (Carl Zeiss MicroImaging, Inc. Oberkochen, Germany), using an Axiocam 503 color (Carl Zeiss MicroImaging, Inc.). The thickness of the inner nuclear layer and the outer nuclear layer was calculated.

Immunohistochemistry: Left eyes were fixed in 4% paraformaldehyde for 2 h at 4 °C and then cryoprotected at 4 °C in a graded series of sucrose. Eyes were embedded in optimal cutting temperature compound (Sakura Finetek), sectioned at 12 µm on a cryostat, mounted on Superfrost glass slides (Fisher Scientific, Waltham, MA), air-dried, and stored at −80 °C until used. Fluorescence immunohistochemistry was used to visualize the retinal layers of neuronal cells and their synapses, assess gliosis, and quantify microglia. For immunohistochemistry on cryostat sections, slides were brought to room temperature and incubated in a blocking solution (PBS, Fisher Scientific, Waltham, MA: 1X; 137 mM NaCl, 2.7mM KCl, 11.9mM phosphates, pH 7.4 with 0.5% Triton X-100 and 2% normal donkey serum) for 20 min. Then, the sections were incubated overnight at 4 °C with the primary antibody against protein kinase C alpha (PKC-alpha, Sigma-Aldrich, St. Louis, MO), postsynaptic density protein 95 (PSD95, UC Davis/NIH NeuroMab Facility, Davis, CA), and ionized calcium-binding adaptor molecule 1 (Iba1, Wako, Richmond, VA). Sections were rinsed in PBS, and incubated with a 1:200 diluted Alexa 488 conjugated secondary antibody (Invitrogen, Carlsbad, CA) and/or Cy3 conjugated secondary antibody (Jackson Immunoresearch, West Grove, PA) for 45 min at room temperature. All sections were imaged on a Zeiss 510 confocal laser scanning system using ZEN software (Carl Zeiss MicroImaging, Inc.).

Assessment of gliosis: Immunohistochemical staining for glial fibrillary acidic protein (GFAP; Thermo Fisher Scientific, Waltham, MA) was performed to determine the presence and extent of retinal Müller cell gliosis and reactive astrocytes. The percentage of GFAP-labeled area occurring in sections immunostained with the GFAP antibody was quantified using the histogram function of ImageJ software (RSB developed by Wayne Rasband, National Institutes of Health, Bethesda, MD) [24].

Apoptosis assay: Terminal deoxynucleotidyl transferase dUTP nicked-end labeling (TUNEL) staining was performed with an ApopTag kit using fluorescein detection (Millipore, Billerica, MA), according to the manufacturer's instructions. Nuclei were counterstained with 4',6-diamidino-2-phenylindole (DAPI), and specimens mounted in ProLong Gold antifade reagent (Thermo Fisher Scientific, Waltham, MA). The number of apoptotic cells per retina 400 µm from the optic nerve was counted to obtain a TUNEL-positive cells value per retina section per mouse.

Quantification of total and activated microglia: Microglia were quantified in retinal cross sections immunostained with the Iba1 antibody (ThermoFisher) using the Cell Counter and Measure and Label functions of ImageJ software. We counted the number of total and activated microglia based on morphology as described by Jonas et al. [25]. Activated microglia were defined as cells with a large soma size and no extending processes. Additionally, total and activated microglia were quantified in wholemounts. Locations were selected such that they were close to the optic nerve without containing a major artery or vein in the viewing frame. Microglial cells were counted at these positions using Iba1 staining (ThermoFisher).

Quantification of vaso-obliteration and neovascularization: Following wholemount staining as previously described [26], vaso-obliteration (VO) quantification was obtained by manually outlining the edges of the VO area. Semiautomated quantification of the neovascularization (NV) area was done by using the SWIFT_NV plugin developed by Stahl et al. to analyze neovascularization on ImageJ software [27].

Statistical analysis: Statistical analyses were performed in GraphPad Prism 6 (GraphPad Software, La Jolla, CA). The statistical difference between groups was calculated using unpaired Student's two-tailed *t* test, and analysis of variance (ANOVA) using the GraphPad Prism software. A p value of less than 0.05 was considered statistically significant, using *p<0.05, **p<0.01, ***p<0.001, and ****p<0.0001. All data are presented as the mean ± the standard error of the mean (SEM) of three or more independent experiments, with three or more replicates per condition per experiment.

RESULTS

In vivo studies of retinal vascularization, structure, and function showed capillary attrition, retinal thinning, and abnormal function: In vivo FA in the OIR mice showed avascular areas in the paracentral retina at P19 and P24, and full peripheral retinal vascularization of the major vessels albeit with a persistently sparse capillary network at P32 and P47. Representative FA images in the RA and OIR mice are shown at P19 and P47 (Figure 1A). Assessment of the RAA showed no statistically significant difference between

the RA and OIR mice at P19 (50.83 ± 3.040% versus 45.8 ± 4.28%, p>0.05, n = 6), P24 (51.50 ± 2.890% versus 59.83 ± 4.090%, p>0.05, n = 6) and P32 (47.80 ± 3.190% versus 52.00 ± 3.680%, p>0.05, n = 6), (p>0.05), but a trend toward more avascularity in the OIR mice at P47 (46.00 ± 1.270% versus 50.33 ± 1.570%, p = 0.0566, n = 6). Representative quantification of the retinal avascular area at P19 and P47 is shown in Figure 1D. In vivo SD-OCT of the OIR mice showed reduced thickness in the avascular areas compared to the hypovascular areas, as previously reported [28]. Representative SD-OCT images in the RA and OIR mice are shown at P19 and P47 (Figure 1B). There was no difference in thickness between the RA and OIR mice at P19 (52.03 ± 2.470 µm versus 55.08 ± 4.740 µm, p>0.05, n = 6) and P32 (43.78 ± 1.030 µm versus 51.15 ± 2.900 µm, p>0.05, n = 6). There was a reduction in the total retinal thickness in the OIR mice compared to the RA mice at P24 (46.28 ± 1.330 µm versus 59.73 ± 2.940 µm, p = 0.0177, n = 6) and P47 (42.93 ± 0.270 µm versus 49.11± 1.850 µm, p = 0.0032, n = 6). The outer retina in the RA mice was of uniform thickness at all ages. The outer retinal thickness in the OIR mice was similar to that of the RA mice at P19, P24 and P32, but thinner at P47 (p = 0.001). The inner retina of the OIR mice was thinner at P19 (p = 0.02) and P47 (p = 0.02) than that of the RA mice. In vivo fERG showed focal areas of abnormalities in rod neuronal responses from the retinas of the OIR mice compared to the retinas of the RA mice (Table 1). Representative fERG images in the RA and OIR mice are shown at P19 and P47 (Figure 1C). fERGs were recorded in response to focal flashes from 0.1 to 3.0 log cd.sec/m^2. There was an increase in the amplitude of the rod photoreceptor-derived part of the fERG, the a-wave, in the P32 OIR mice compared to the P32 RA mice at the lowest flash intensity, 0.1 log cd.sec/m^2 (p = 0.003); otherwise, the a-wave amplitude was relatively unchanged between the OIR and RA mice. Conversely, there was a statistically significant loss of amplitude of the post-photoreceptor neural responses, the b-wave, in the P32 OIR mice at low intensity (p<0.01) compared to the age-matched RA mice, and in the P47 OIR mice compared to the age-matched RA mice at moderate, 0.30 log cd.sec/m^2, (p = 0.003), 1.0 log cd.sec/m^2 (p = 0.02), and high, 3.0 (p = 0.01) log cd.sec/m^2 flash intensities. The a-wave peak times were decreased at P19 only at the higher intensities 1.0 (p<0.01) and 3.0 log cd.sec/m^2 (p = 0.02). The b-wave peak times had a trend toward reduction in the OIR mice at P19 at moderate intensity, 0.30 log cd.sec/m^2, compared to the age-matched RA mice (p = 0.057; Table 1). In summary, these studies of retinal vascularization, structure, and function demonstrated persistent abnormalities until adulthood (P47) in the OIR mice.

Retinal histological cross sections showed reduced inner retinal thickness in a patchy pattern: We observed disorganization in the structure and morphology of the retinal layers in the OIR mice compared to the RA controls at all time points studied: P19, P24, P32, and P47, (Figure 2A–C). The thickness of the inner and outer nuclear layers was measured 200 µm from the optic nerve up to 2,000 µm peripherally, at 200 µm intervals and presented in Table 2. The ganglion cell layer (GCL), inner plexiform layer (IPL), inner nuclear layer (INL), and outer plexiform layer (OPL) of the OIR mice exhibited thinning in a patchy pattern compared to the corresponding layers in the RA mice which showed consistent thickness (Figure 2 A,B). This was especially notable in the inner nuclear layer, which in some areas appeared to be about three cell layers in thickness in the OIR mice compared to about six or more layers of thickness in RA mice (Figure 2B). These structural abnormalities appeared to be patchy in appearance along the circumferential length of the retina, with the peripheral retina more abnormal than the central retina, and the presence of mildly affected or near-normal areas along the length of the retinal cross section. We also observed an increase in blood vessels present in the OIR mouse retina compared to the RA mouse retina, which was more prevalent near the peripheral retina (Figure 2C). Additionally, the outer plexiform layer, which contains synapses, was thinner and disorganized in the OIR mice compared to that of the RA mice (Figure 2A,B). The INL in the OIR mice was statistically significantly thinner than that of the RA mice at P19 when measured at 600, 800, and 1,200 µm. There was no difference in the INL of the RA and OIR mice at P24 or P32, at the intervals measured. However, by P47, the INL was statistically significantly thinner in the OIR mice compared with the RA mice at 400, 600, and 2,000 µm. The ONL of the OIR mice was thicker than that of the RA mice only at 1,200 µm at P47; otherwise, there was no difference in the ONL between the RA and OIR mice at any age or in any retinal cross section measured. Although the overall differences between the inner and outer retina were not statistically significantly different between the RA and OIR mice in each retinal cross section measured, likely due to the patchy nature of the phenotype, there were data points that exhibited statistically significant thinning in the OIR retina (Figure 2B), most notable in the peripheral retina (Table 2). Physiologically, the ONL was thicker than the INL in the RA mice in several cross-sectional areas at P19 and P47, but there was no difference between the ONL and the INL in the OIR mice at P19 and P47, a reflection of a decrease in the ONL thickness to become equivalent in thickness to the INL in the OIR mice. Retinal histology sections showed an increase in angiogenic activity in the peripheral retina

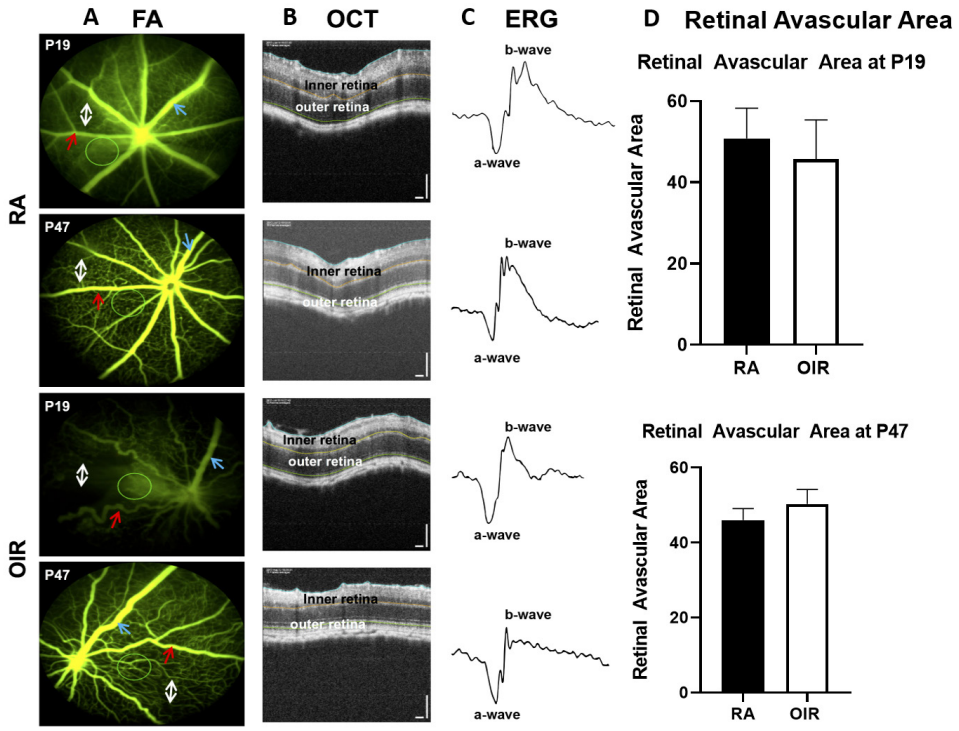

Figure 1. In vivo imaging in RA and OIR mice. **A**: Representative fluorescein angiography, FA, at P19 and P47 in RA and OIR mice. FA shows uniform capillaries, veins, and arteries in the RA mice. FA shows the avascular capillary network in the OIR mice compared to the RA mice at P19, and a persistent sparse capillary network in the OIR mice compared to the RA mice at P47. The capillary network (white double arrow) is dense in the RA mice and sparse in the OIR mice. There are dilated veins and tortuous arteries in the OIR mice, and veins (blue arrows) and arteries (red arrows). Green circles in the FA images indicate the region of interest (ROI) where electroretinogram (ERG) and spectral domain optical coherence tomography (SD-OCT) measurements were obtained. **B**: Representative SD-OCT shows a thinner inner retina in the OIR mice compared to the RA mice at P19 and P47. **C**: Representative ERGs at P19 and P47 in the RA and OIR mice. The ERG shows a decrease in the b-wave amplitude at P47 in the OIR mice compared to the RA mice. **D**: Quantification of the retinal avascular area. The retinal avascular area (empty spaces in between capillaries and major vessels in the RA and OIR mice) was quantified as a percentage (%) of the total retinal area, using an automated MATLAB program, as previously published [22]. Although the OIR phenotype showed capillarity avascularity at P19 and sparsity at P47, the quantification of the retinal avascular area from the FA images in Figure 1A did not show a statistically significant difference between RA and OIR mice at P19 (50.83 ± 3.040% versus 45.8 ± 4.28%, p>0.05, n = 6), but showed a trend toward more avascularity in the OIR mice at P47 (46.00 ± 1.270% versus 50.33 ± 1.570%, p = 0.0566, n = 6). Representative images of simultaneous FA, SD-OCT, and ERG are shown in Figures 1A–C. RA = room air; OIR = oxygen-induced ischemic retinopathy; P = postnatal day. Six RA mice and six OIR mice were examined for each developmental age studied. A p value of less than 0.05 was considered statistically significant.

with developmental maturity, but a decrease in inner retinal thickness. This was more evident in the inner nuclear layer, containing cell bodies of the bipolar cells, horizontal cells, and amacrine cells. In addition, subtle decreases in the outer nuclear layer thickness in OIR mice, where the cell bodies of the photoreceptor cells are contained, were noted.

Ectopic localization of photoreceptor cell synapses in the retinas of OIR mice: To observe the integrity of the synaptic connections following oxidative stress, we performed immunohistochemical staining of the photoreceptor presynaptic terminals using the PSD95 antibody (in green) and the rod bipolar cells using the PKC-alpha antibody (in red). The RA mice showed well-aligned and apposed synapses, but the OIR mice demonstrated fewer, disorganized and mal-aligned or ectopic synapses at all time points (Figure 3A). We observed abnormal extension of the bipolar cell dendrites from the OPL into the ONL (PKC-alpha antibody; red in Figure 3A, white in Figure 3B) and ectopic localization of photoreceptor presynaptic terminals (PSD95; green in Figure 3A) in the OIR mice. This phenotype does not occur in a peripheral to central manner as observed in mature mice [29], but in a patchy pattern throughout the retina. Quantification of the ectopic dendrites per 200 µm showed a significant increase in the number of dendrites in the OIR mice compared to the RA mice at every developmental age in the central and peripheral retina, but there was no difference within either group with increasing age, Figure 3C, Table 3. Quantification of the PKC-alpha stained bipolar cells showed a significant difference between the RA and OIR mice at every age tested in the peripheral retina, but did not show a difference in the central retina between the RA and OIR mice. There was no difference in PKC-alpha stained bipolar cells with increasing age, Figure 3C, Table 3. These data suggest that the synaptic

Table 1. ERG parameters at increasing light flash intensities per postnatal day age.

Age	RA					OIR				
	n	0.1†	0.3 †	1.0 †	3.0 †	n	0.1 †	0.3 †	1.0 †	3.0 †
a-wave Amplitude										
P19	6	−5.7±1.33	−9.3±2.86	−10.3±1.027	−64.4±9.72	5	−10.5±3.18	−13.9±5.032	−13.9±1.46	−56.8±11.33
P24	6	−6.7±2.58	−4.3±2.16	−8.4±2.58	−46.6±11.43	6	−7.8±1.96	−6.2±1.73	−9.5±2.33	−51.4±9.20
P32‡	5	−9.7±1.02‡	−5.5±1.23	−10.8±4.27	−49.7±7.16	6	−3.4±1.18‡**	−5.1±0.81	−3.4±0.93	−48.7±5.75
P47	6	−7.8±1.18	−8.9±2.27	−5.3±1.30	−48.9±6.24	6	−4.9±0.82	−4.3±1.14	−4.5±1.68	−46.2±7.75
b-wave Amplitude										
P19	6	19.5±3.55	29.5±4.40	48.0±8.0	159.0±23.53	5	14.3±1.99	19.6±5.79	30.1±6.51	95.6±22.38
P24	6	15.2±1.65	23.6±3.28	42.1±8.4	125.5±18.77	6	13.9±2.34	21.5±5.55	29.6±2.81	94.5±11.65
P32‡	5	18.9±2.50	31.1±7.57	42.8±9.2	130.6±15.68	6	8.7±1.62‡**	16.2±1.80	28.0±3.72	97.2±11.57
P47‡	6	17.6±2.34	30.0±2.81‡	47.2±6.09‡	129.6±10.93‡	6	18.7±3.60	15.0±2.53‡**	26.9±3.87‡*	76.5±13.52‡**
a-wave Peak Times										
P19‡	6	42.63±14.71	52.1±16.10	34.8±7.01‡	29.8±0.50‡	5	56.4±15.02	58.8±15.28	64.2±4.38‡*	34.4±1.64‡**
P24	6	52.27±15.57	23.5±10.32	41.8±8.78	34.7±2.06	6	49.5±14.47	43.6±14.05	54.2±8.08	38.4±6.89
P32	5	70.3±8.61	29.7±15.24	42.0±4.87	30.44±2.07	6	33.7±15.37	31.5±10.53	32.87±6.62	32.9±0.85
P47	6	66.9±4.83	27.6±4.49	21.3±7.54	32.0±0.79	6	60.8±20.05	25.1±15.09	42.6±11.61	32.6±1.19
b-wave Peak Times										
P19‡	6	72.9±24.17	126.6±3.53‡	111.5±3.41	79.0±3.57	5	85.9±31.10	82.2±22.14‡*	128.3±8.56	92.5±6.58
P24	6	121.3±12.05	125.1±7.47	120.5±6.80	75.7±8.38	6	135.7±8.84	115.5±18.79	122.4±4.97	73.8±8.40
P32	5	105.2±23.53	97.4±15.60	104.5±8.81	63.6±2.99	6	88.6±17.07	125.8±4.70	114.8±3.89	66.1±1.44
P47	6	126.4±9.11	112.9±2.16	100.8±3.82	61.9±3.77	6	92.6±19.12	116.7±12.99	110.2±3.48	72.1±4.64

Note: All values are presented as mean ± SD. ERG denotes Electroretinogram; RA denotes room air; OIR denotes oxygen-induced ischemic retinopathy; P denotes postnatal day age; n denotes number of mice per age. † denotes flash light intensities in log cd.sec/m^2; ‡ denotes age with statistically significant results presented as follows: Asterisks (*) refers to p values: * refers to p<0.05, ** refers to p<0.01, *** refers to p<0.001, **** refers to p<0.0001.

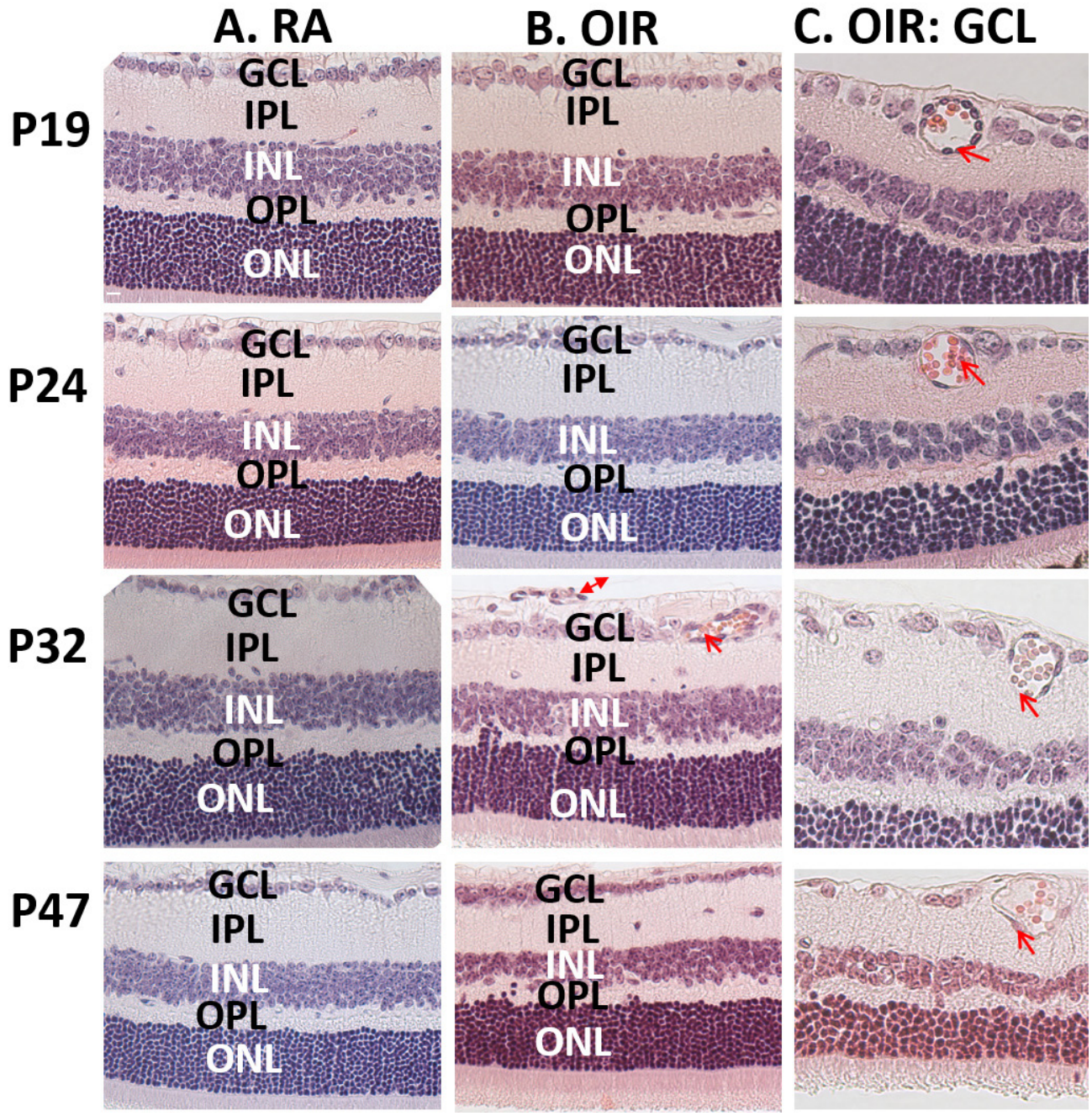

Figure 2. Retinal thickness analysis at P19, P24, P32, and P47 in RA and OIR mice. **A**: H&E cross sections of retinas of the RA mice. Histology shows normal architecture at P19 and P47. **B**: Retinal cross section of the OIR mice. Histology shows neovascularization (red arrow) at P1, inner retinal thinning, and disorganized retina architecture, particularly the outer retina. Neovascularization above the inner limiting membrane is shown with a red double arrow. **C**: OIR mice showing dilated blood vessels (red arrow) in the GCL. H&E shows an increase in the blood vessel number and dilation in the OIR mice and the disorganized OPL. H&E = hematoxylin & eosin; RA = room air; OIR = oxygen-induced ischemic retinopathy; P = postnatal day; GCL = ganglion cell layer, INL = inner nuclear layer; IPL = inner plexiform layer; OPL = outer plexiform layer; ONL = outer nuclear layer. Three RA mice and three OIR mice were examined for each developmental age studied.

Table 2. Inner nuclear layer and outer nuclear layer values in RA and OIR mice.

INL and ONL	P19		P24		P32		P47	
	RA (n=3)	OIR (n=3)	RA (n=3)	OIR (n=3)	RA (n=3)	OIR (n=3)	RA (n=3)	OIR (n=3)
200 µm								
INL	33.99±1.8	29.91±3.32	37.26±7.3	34.93±3.0	27.55±3.5	26.11±7.5	32.77±2.8‡	21.66±7.5‡**
ONL	44.88±2.5 †*	42.34±1.92 †**	52.3±3.3	55.53±9.9	37.17±6.3	43.00±9.05	47.43±1.3 †****	45.60±1.1
400 µm								
INL	39.21±0.9	33.21±6.37	39.29±2.1	30.74±4.8	28.68±2.4	21.28±3.8	32.58±4.9‡	18.99±9.7‡***
ONL	54.42±1.03 †**	50.64±4.61 †****	54.01±6.3	52.18±6.8	43.08±2.3	44.69±6.1	46.84±2.1 †***	47.93±1.3
600 µm								
INL	43.84±1.9‡	27.05±1.98‡****	40.98±4.9	31.88±7.6	31.33±4.4	20.73±3.2	31.13±0.5	23.03±3.4
ONL	53.40±1.9	47.51±6.23 †****	52.00±0.5	55.21±11.8	47.51±3.9 †**	47.15±6.4	42.95±3.9 †**	47.22±1.3
800 µm								
INL	41.03±5.1‡	26.45±4.13‡***	41.39±1.8	36.83±10.2	31.74±5.1	21.33±2.7	31.93±2.3	27.29±1.0
ONL	53.25±2.7 †****	48.05±3.08 †****	55.31±1.5	48.74±10.0	44.4±8.2	48.00±6.2	43.56±1.0 †**	48.29±0.5
1000 µm								
INL	38.04±2.5	29.53±1.06	36.74±4.8	29.12±3.6	30.18±6.3	23.31±1.3	28.67±1.5	25.23±1.3
ONL	54.58±2.4†**	46.1±3.99†****	52.27±2.4	46.36±5.4	45.58±11.1	47.67±8.3	43.44±1.0 †****	49.21±0.4
1200 µm								
INL	39.27±2.9‡	28.06±5.45‡*	35.23±3.0	27.00±2.9	29.89±9.1	27.85±3.2	27.24±2.9	25.32±3.4
ONL	51.58±1.9 †****	45.72±3.41 †****	55.7±6.6	48.29±3.5	44.9±7.4	47.50±4.8	41.27±8.1‡***	54.51±5.7‡***
1400 µm								
INL	33.05±2.4	29.36±6.68	37.99±2.4	25.68±1.1	30.88±3.2	26.67±6.3	27.67±2.3	28.89±3.1
ONL	51.23±1.4 †****	44.5±2.87 †****	54.42±7.5	46.79±7.9	43.81±4.7*	47.58±8.3	44.36±4.5 †****	44.27±3.2
1600 µm								
INL	33.35±6.9	26.4±3.34	35.02±3.9	21.27±4.3	27.27±2.7	25.41±8.6	24.83±1.3	21.20±0.7
ONL	49.77±2.2 †****	44.12±6.03 †****	51.42±8.4	44.00±4.6	40.27±3.5	49.10±6.2	41.69±4.4 †****	41.43±2.7
1800 µm								
INL	33.70±5.4	25.18±5.03	32.62±7.2	19.54±0.5	27.47±2.7	24.03±4.1	27.59±4.8	19.18±1.2
ONL	48.26±3.7 †***	43.19±6.51 †****	47.29±6.9	43.55±4.0	40.73±6.7	45.47±9.4	40.27±4.0 †**	41.78±2.8
2000 µm								
INL	29.95±4.4	20.37±4.9	30.49±4.8	19.14±0.4	29.21±3.3	19.52±10.7	26.31±3.8‡**	15.44±0.4‡**
ONL	44.86±1.2 †***	36.37±7.35 †****	43.92±8.0	32.54±9.1	40.92±3.9	39.56±14.4	37.14±4.8 †*	38.81±5.0

Note: All values are presented as mean±SD. RA denotes room air, OIR denotes oxygen-induced ischemic retinopathy, P denotes postnatal day age; INL denotes inner nuclear layer, ONL denotes inner nuclear layer. P values between RA and OIR mice are stated in the table. † denotes significance between INL and ONL values per measured cross-

sectional distance from optic nerve for either RA or OIR mice. ‡ denotes significance between RA and OIR mice per measured cross-sectional distance from optic nerve. Asterisks (*) refers to p values: * refers to p<0.05, ** refers to p<0.01, *** refers to p<0.001, **** refers to p<0.0001

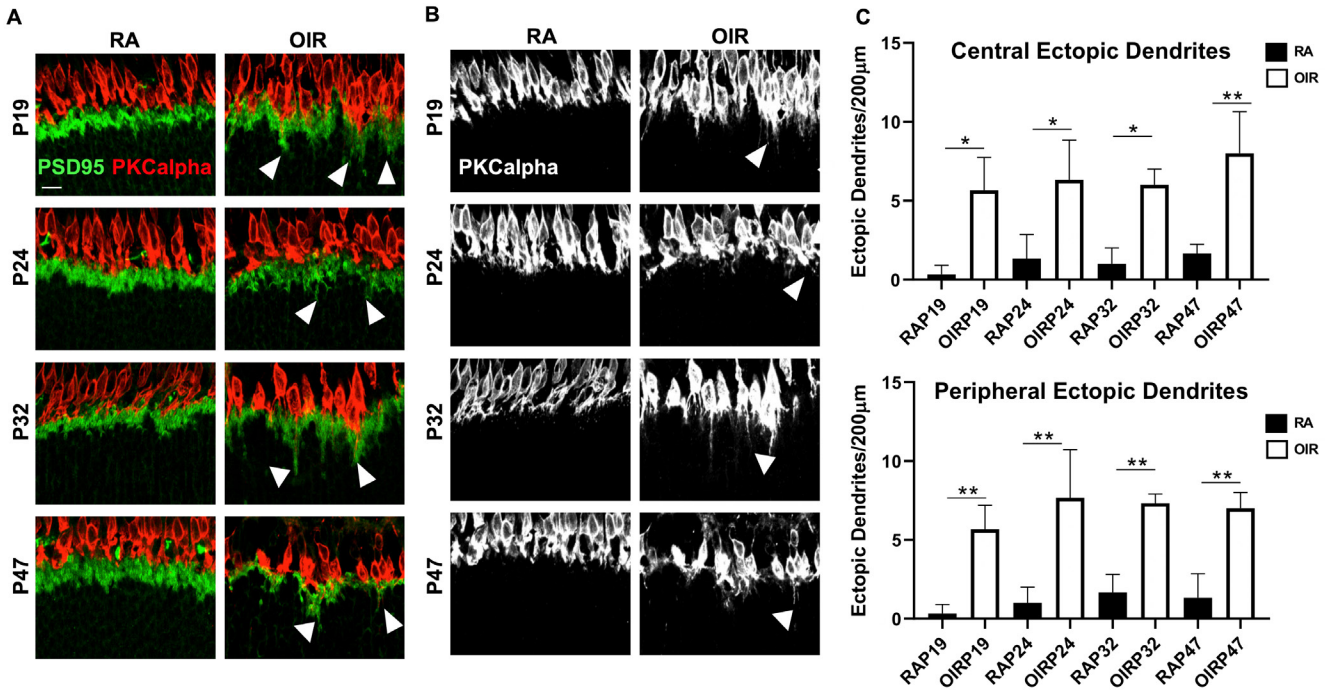

Figure 3. Synaptic morphology at P19, P24, P32, and P47 in RA and OIR mice. **A** and **B**: Immunohistochemistry showing ectopically aligned synapses between photoreceptor presynaptic terminals and rod bipolar cells in the OPL from retinal cross sections at P19, P24, P32, and P47. PKC-alpha (red in **A**, white in **B**) stains rod bipolar cells, and PSD95 (green in **A**) stains photoreceptor presynaptic terminals. **C**: Quantification of ectopic dendrites per 200 µm in the central and peripheral retina. The white arrow heads in **A** and **B** point to ectopically localized synapses extending beyond the OPL. RA = room air; OIR = oxygen-induced ischemic retinopathy; P = postnatal day; OPL = outer plexiform layer; PSDS = postsynaptic density protein; PKC-alpha denotes protein kinase c alpha. Three RA mice and three OIR mice were examined for each developmental age studied. Stars denote level of significance: *p < 0.05, **p < 0.01, ***p < 0.001, and ****p < 0.0001. Sampling size: n=3 for each group. Error bars represent SEM.

connections of photoreceptor cells and the quantity of photoreceptor cells are disrupted in the OIR retina, particularly in the peripheral retina.

Apoptosis in retinas of OIR mice: To determine the presence and duration of apoptotic cell death in the OIR retina, we performed TUNEL staining on the OIR and RA mice at all four time points (P19, P24, P32, and P47) at a location 400 µm from the optic nerve. There was a significant increase in TUNEL positive signals (green) in the OIR mice compared to the RA mice at all time points (Figure 4A,B). The highest number of TUNEL-positive cells was observed at P19, with decreasing severity into adulthood at P47. Apoptosis in the OIR retina, although less severe at P47, was still statistically significantly more apparent than in the age-matched RA mice, signifying persistent ongoing cell death in the OIR mice. In addition, we quantified the TUNEL positive cells by retinal cell layer (Table 4), showing that apoptosis was most significant in the GCL and the ONL of the OIR mice at P19, and persisted only in the ONL of the OIR mice at P24. The TUNEL positive cells in the OIR mice had variable severity at every age tested (zero to nine cells), such that it was not statistically different from that of RA mice (zero to three cells). Thus, there was increased apoptosis in the OIR mice compared to the RA mice, which decreased with increasing developmental age, but persisted into adulthood.

OIR mice showed increased gliosis: To determine the time course and duration of gliosis in the OIR retina, GFAP staining was performed. There was increased intensity of GFAP staining in the retinas of the OIR mice in comparison to the retinas of the RA mice indicating gliosis. GFAP-positive astrocytes were observed in the nerve fiber layer, just below the inner limiting membrane of the RA and OIR mice (Figure 5A). The GFAP signals in this layer appeared more prominent in the OIR mice than in the RA mice (Figure 5A) suggesting reactive changes in the astrocytes [30]. The cell bodies of Müller cells are typically located in the inner nuclear layer, and span the entire retinal cross section from the inner limiting to the outer limiting membrane. There was no GFAP staining of Müller cells in the RA mice at any time points (Figure 5A), but there was GFAP staining in the Müller

Table 3. Quantification of PKC-alpha positive cells and ectopic dendrites per postnatal day age.

Cells and dendrites	P19		P24		P32		P47	
Number per 200 µm	RA (n=3)	OIR (n=3)	RA (n=3)	OIR (n=3)	RA (n=3)	OIR (n=3)	RA (n=3)	OIR (n=3)
PKC-alpha positive cells	39.33±8.6	30.67±0.6	37.67±6.4	28.67±1.2	33.33±1.5	28.33±2.1	32.00±3.6	25.33±2.3
Ectopic Dendrites	0.33±0.6†	5.67±2.1†*	1.33±1.5†	6.33±2.5†*	1.00±1.0†	6.00±1.0†*	1.67±0.6†	8.00±2.6†**
PKC-alpha positive cells	35.67±3.5†	27.67±2.1†*	39.00±2.7†	28.33±2.5†**	34.00±1.0†	27.67±3.2†*	35.67±3.5†	23.67±1.5†**
Ectopic Dendrites	0.33±0.6†	5.67±1.5†**	1.00±1.0†	7.67±3.1†**	1.67±1.2†	7.33±0.6†*	1.33±1.5†	7.00±1.0†**

Note: All values are presented as mean±SD. RA denotes room air; OIR denotes oxygen-induced ischemic retinopathy; P denotes post-natal day age; n denotes number of mice per age; PKC-alpha denotes protein kinase C alpha. P values between RA and OIR mice are stated in the table. † denotes significance between RA and OIR mice per measured cross-sectional distance from optic nerve. Asterisks (*) refers to p values: * refers to p<0.05, ** refers to p<0.01, *** refers to p<0.001, **** refers to p<0.0001

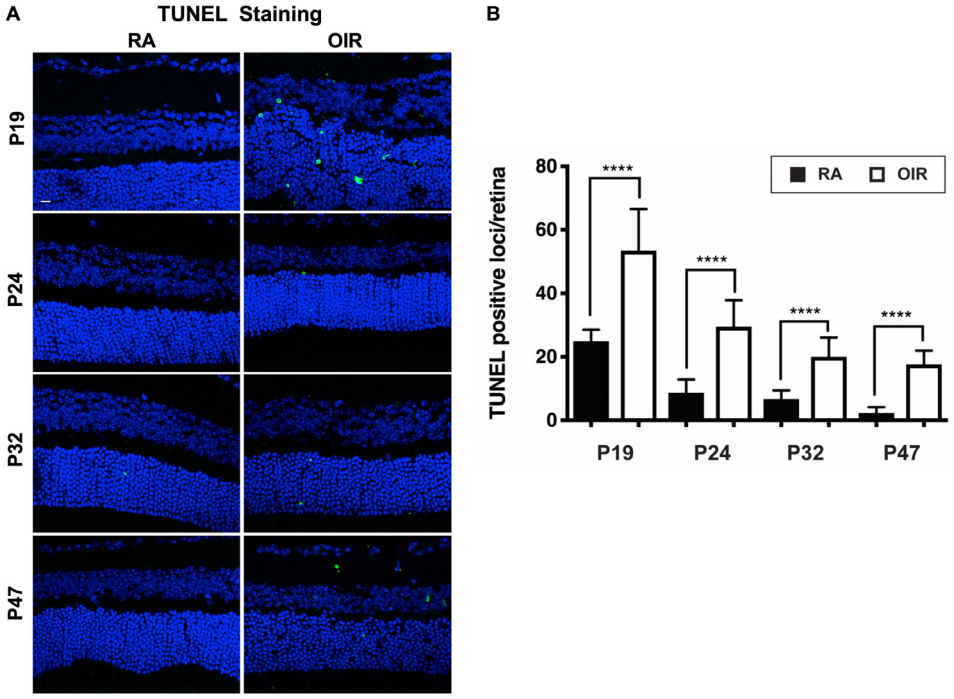

Figure 4. Apoptosis at P19, P24, P32, and P47 in RA and OIR mice**.** **A**: TUNEL staining for apoptosis shows increased apoptosis in the OIR mice compared to the RA mice. **B**: Quantification of TUNEL staining in RA and OIR mice with increasing developmental age. RA = room air; OIR = oxygen-induced ischemic retinopathy; P = postnatal day; TUNEL = terminal deoxynucleotidyl transferase dUTP nicked-end labeling. Three RA mice and three OIR mice were examined for each developmental age studied. Stars denote level of significance: *p< 0.05, **p< 0.01, ***p< 0.001, and ****p< 0.0001. Sampling size: n=3 for each group. Error bars represent SEM.

cells of the OIR mice compared to the RA mice at every time point measured. However, there was no statistically significant increase in the GFAP staining of the Müller cells with advancing development age in the OIR mice. This is also depicted in the quantification of GFAP positive staining in the RA and OIR mice (Figure 5B). Thus, we observed reactive changes in astrocytes and Müller cell gliosis in the OIR mice, which persisted into adulthood.

OIR mice showed increased activation of microglia: Microglia activation was present in the OIR mice and persisted throughout adulthood. We observed a statistically significant increase in the number of total microglia in the retinas of the OIR mice compared to the retinas of the RA mice in the retinal flatmounts (Figure 6A,B). At P19, very few Iba1-positive microglia (green) were observed in the RA mice. Statistically significantly increased numbers of Iba1-positive microglia were observed in the OIR mice,

Table 4. Quantification of TUNEL positive cells per postnatal day age.

Retinal layers	P19		P24		P32		P47	
	RA (n=3)	OIR (n=3)	RA (n=3)	OIR (n=3)	RA (n=3)	OIR (n=3)	RA (n=3)	OIR (n=3)
GCL	0±0†	3±1†***	0±0	1±1	0±1	2±1	0±1	2±1
INL	0±1	1±0	1±0	1±1	0±1	0±1	0±0	1±2
OPL	0±0	1±0	0±0	0±0	0±0	0±0	0±0	1±2
ONL	2±1†	6±3†****	1±1†	3±1†**	1±0	3±1	0±1	1±1
RPE	0±1	2±1	0±0	0±1	0±0	0±1	0±0	1±0

Note: All values are presented as mean±SD. RA denotes room air; OIR denotes oxygen-induced ischemic retinopathy; P denotes postnatal day age; n denotes number of mice per age; TUNEL denotes Terminal deoxynucleotidyl transferase dUTP nicked-end labeling. GCL denotes Ganglion cell layer; INL denotes inner nuclear layer; IPL denotes inner plexiform layer; OPL denotes outer plexiform layer; ONL denotes outer nuclear layer; RPE denotes retinal pigment epithelium. P values between RA and OIR mice are stated in the table. † denotes significance between RA and OIR mice per measured cross-sectional distance from optic nerve. Asterisks (*) refers to p values: * refers to p<0.05, ** refers to p<0.01, *** refers to p<0.001, **** refers to p<0.0001. All values are measured at 400µm form the optic nerve.

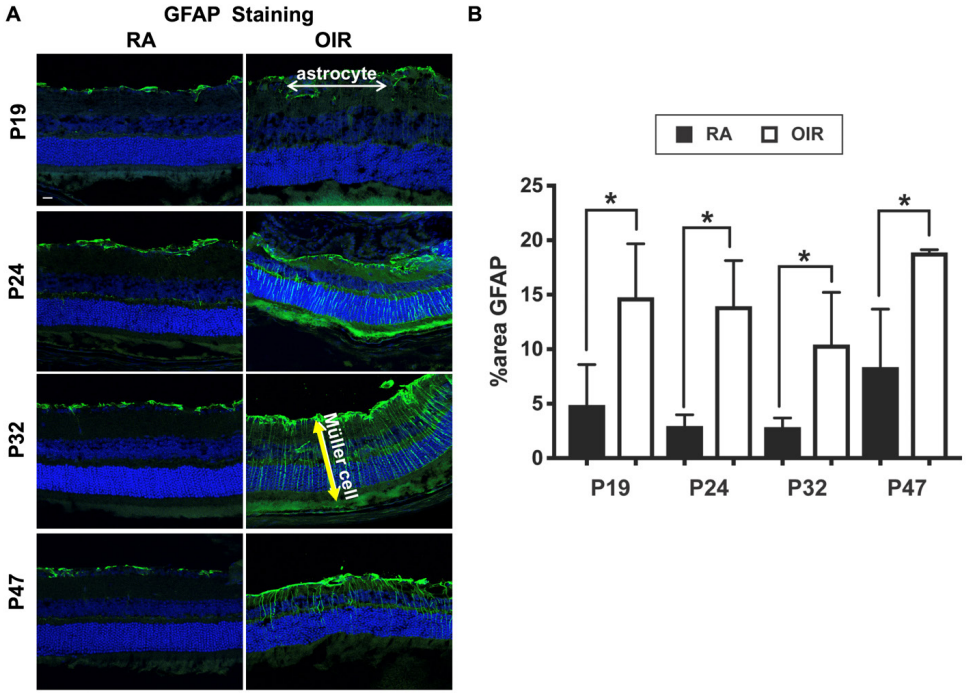

Figure 5. GFAP staining at P19, P24, P32, and P47 in RA and OIR mice. **A**: GFAP staining in RA mice. **B**: GFAP staining in OIR mice. White double arrow shows astrocyte location in the nerve fiber layer. Yellow double arrow head shows Müller cell location spanning the entire retinal cross section. **C**: Quantification of GFAP expression in RA and OIR mice with increasing developmental age. RA = room air; OIR = oxygen-induced ischemic retinopathy; P = postnatal day; GFAP = glial fibrillary acidic protein. Three RA mice and three OIR mice were examined for each developmental age studied. Stars denote level of significance: *p< 0.05, **p< 0.01, ***p< 0.001, and ****p< 0.0001. Sampling size: n=3 for each group. Error bars represent SEM.

most abundant at P19 and P24, with decreasing severity in the mature mice, but still persisting at P47 in the OIR mice. Although a stable number of Iba1-positive microglia were observed in the RA mice at every age tested, an increased number of active microglia (Figure 6D) with their larger soma size and absent dendrites (Figure 6B, white arrows) [25] were observed in the OIR mice compared to the RA mice (Figure 6A).

Retinal flatmounts were prepared to further assess the morphology of the microglia in the RA and OIR mice (Figure 7A). Total and activated microglia numbers were confirmed as increased in the OIR mice (n = 4) compared with the RA mice (n = 4), showing a statistically significantly higher number of total and activated microglial cells in OIR mice at all developmental ages tested (Figure 7B).

Retinal wholemounts showed an increase in vaso-obliteration and neovascularization in the OIR mice at P19: Retinal wholemounts were prepared in the RA and OIR mice (Figure 8A) to compare with the in vivo retinal vascular imaging findings. In the RA mice, there were no quantifiable areas of vaso-obliteration and neovascularization, while the OIR mice showed decreasing areas of vaso-obliteration and neovascularization with advancing age (Figure 8B). Thus, a value of 0.000001% was assigned for one sample in the RA mice to enable numerical quantification. At P19, compared to the RA mice (n = 4), the OIR mice (n = 4) had a percent area of vaso-obliteration compared to the total retinal area of 11.32 ± 5.820%, p = 0.008; while the percent area of neovascularization was 9.18 ± 3.38%, p = 0.002. At P24, there was no difference in percent vaso-obliteration (0.42 ± 0.43% versus 0%, p = 0.16) and neovascularization (0.45 ± 0.37% versus 0%, p = 0.16) between the OIR mice (n = 4) and the RA mice (n = 3), respectively. At P32, although vaso-obliteration was statistically significantly increased in the OIR mice (n = 4) compared to the RA mice (n = 3) (0.07 ± 0.05% versus 0%, p = 0.04), there was no difference in neovascularization (p = 1) in the two groups of mice. At P47, there was no difference in percent vaso-obliteration (0.03 ± 0.07% versus 0%, p = 0.4) and neovascularization (p = 1) between the OIR mice (n = 4) and the RA mice (n = 3) mice, respectively. Persistent vaso-obliteration was observed in the flatmounts of the adult OIR mice despite full revascularization.

DISCUSSION

OIR studies typically focus on evaluating therapies to mitigate abnormal vascularization [31,32]; however, the persistence of functional deficits in patients with treated or regressed ROP beyond childhood [8,10,33] raises concerns about the long-term effects of hyperoxia on other retinal phenotypes. The aim of this study was to determine the duration and severity

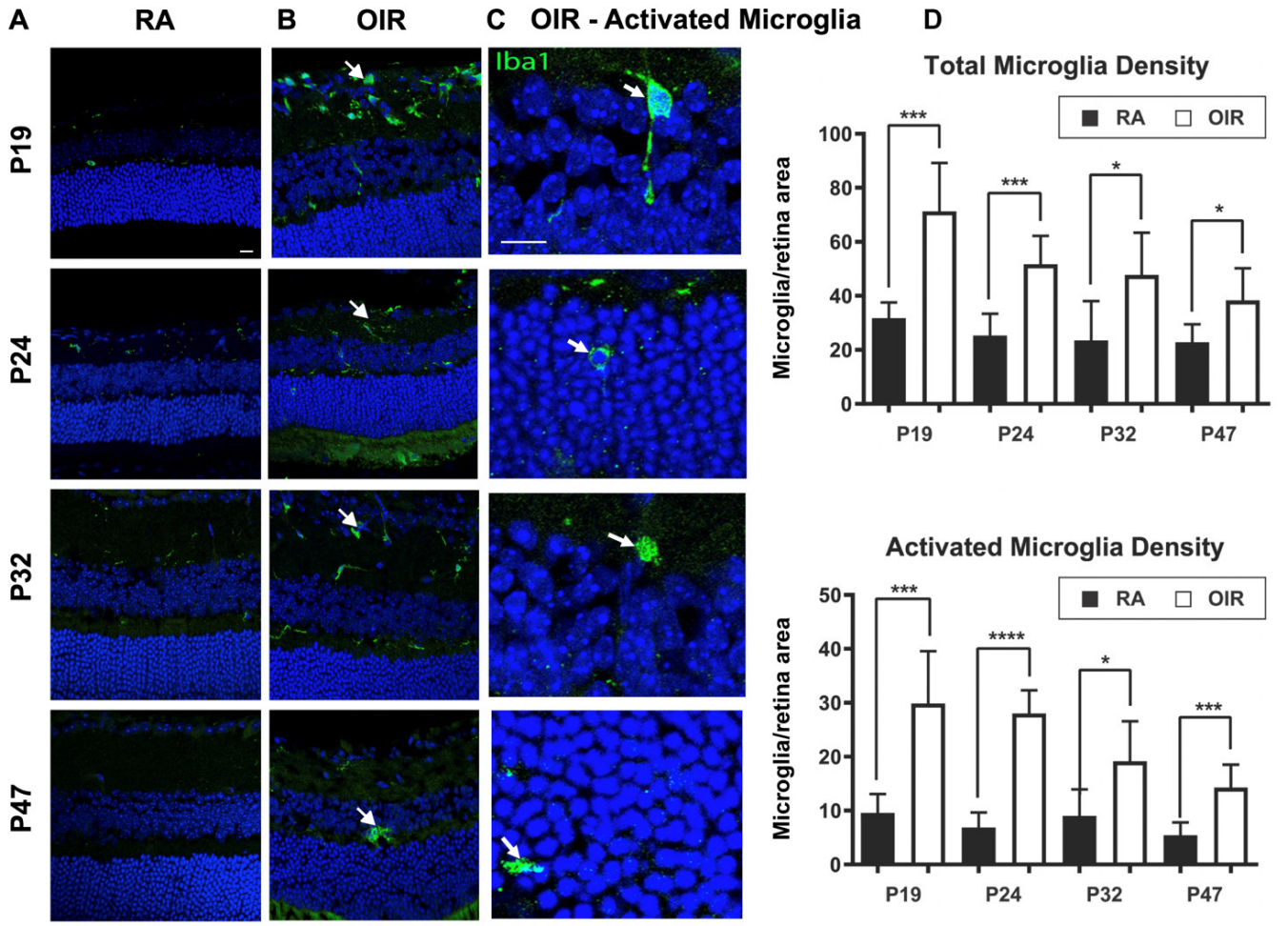

Figure 6. Activated microglia activity at P19, P24, P32, and P47 in RA and OIR mice. **A**: Iba1 staining in the retinas of the RA mice. **B**: The white arrow denotes activated microglia. **C**: Activated microglia in OIR mice (magnified view from each age in **B**). **D**: Quantification of total microglial cells and activated microglial cell densities. Three RA mice and three OIR mice were examined for each developmental age studied. RA = room air; OIR = oxygen-induced ischemic retinopathy; P = postnatal day. Stars denote level of significance: *p< 0.05, **p< 0.01, ***p< 0.001, and ****p< 0.0001. Sampling size: n=3 for each group. Error bars represent SEM.

of multiple retinal phenotypes caused by neonatal hyperoxia in OIR mice. We performed in vivo FA, SD-OCT, and fERG analyses as well as histological analyses of the retinas of OIR mice at time points corresponding to different phases of retinal vascular development. From these analyses, we found that activation of glial cells, abnormal retinal structure and function, progressive retinal cell degeneration, and ectopic photoreceptor synapses are observed from young age until adulthood in OIR mice.

Glia activation was increased throughout retinal vascularization and persisted in the adult OIR mice: Retinal vascularization in mice begins, as in human infants, from the optic nerve and advances peripherally. In OIR mice, exposure to hyperoxia from P7 to P12 causes an avascular central zone akin to the vaso-obliterative phase of ROP in human infants. After the OIR mice return to room air, retinal hypoxia develops leading to abnormal revascularization with capillary attrition. The present study, as well as published studies, showed this phenotype using in vivo imaging in neonatal and adult OIR mice. We found that during the same time course, the retinal glial cells, including Müller cells and microglia, remained activated in OIR mice. Although glial cell activation has been observed in other studies, showing gliosis of astrocyte and Müller cells and increased microglia activation in OIR mice soon after exposure to hyperoxia [15-17,34], the present study uniquely showed that glial activation persists as late as P47 in OIR mice.

Glial activation is a physiologic response in a healthy retina exposed to injury or stress, which is normally limited in scope and duration. Microglia when activated during

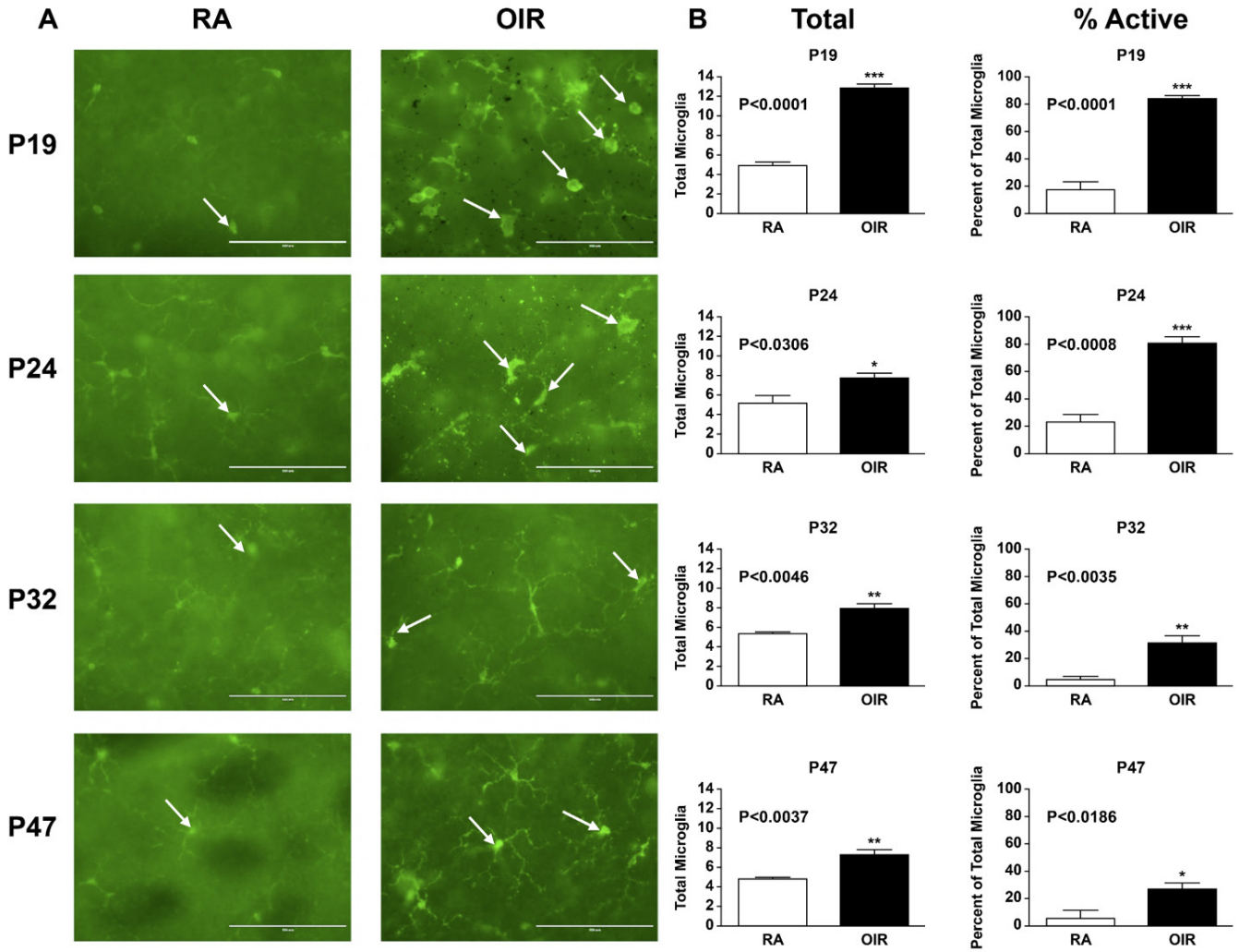

Figure 7. Retinal wholemount of total and activated microglia in RA and OIR mice. **A**: Iba1 staining in the retinas of RA mice and OIR mice. The white arrow denotes activated microglia. **B**: Quantification of total microglial density and percent active microglial. RA = room air; OIR = oxygen-induced ischemic retinopathy; P = postnatal day. Four RA mice and four OIR mice were examined for each developmental age studied. Stars denote level of significance: *p< 0.05, **p< 0.01, ***p< 0.001, and ****p< 0.0001. Sampling size: n=4 for each group. Error bars represent SEM.

apoptosis act as scavengers to remove tissue debris; in contrast, following subtle injury, microglia exhibit a surveillance and protective role [14]. Whether glial cells return to a quiescent stage once the injury has been repaired or noxious stimuli are terminated has not been previously evaluated. The present study showed that glial cells in OIR mice remained activated throughout the observation period into the adult stage, coinciding with the finding of persistent apoptosis in the retina. An increase in GFAP signals indicating Müller cell gliosis and reactive astrocytes was observed as the OIR mice aged. For the mechanism underlying the prolonged activation of glial cells in OIR mice, we propose a two-hit model. While mice are exposed to increased levels of oxygen (P7–P12), glial cells become activated in response to hyperoxia. Once mice are moved to room air on P12, we hypothesize that the retinal glial cells undergo a second stress from the ensuing relative hypoxia due to the inadequate blood supply to the avascular area of the retina before recovering from the previous activation. Previous studies showed that glia cells are activated by hyperoxia and hypoxia [15-17,35-38], supporting the present model. As glial activation is known to correlate with various retinal abnormalities [11], prolonged glial activation in the OIR retina may affect other retinal phenotypes. For example, Müller cells have been shown to guide blood vessel growth into the inner retina by expressing angiogenic growth factors [36]. It is possible that reactive Müller cells undergo a

pathologic alteration in their regulation of angiogenic activity, leading to incomplete and aberrant vascular recovery with sparse capillary density and lingering arterial tortuosity as we observed in adult OIR mice in previous studies.

Müller cells are also known for their homeostatic and metabolic neuron-supportive functions, which become dysregulated in gliotic Müller cells [11]. Müller cells span the entire thickness of the retina and ensheath all retinal neurons, extending numerous branches to the synaptic layers of the retina that surround the neuronal synapses [11]. If Müller cells provide structural stability to the synapses, it is possible that gliotic changes in these cells contribute to the structural abnormalities of the synapses observed in OIR mice. The present finding of GFAP staining in a vertically linear pattern corresponding to Müller cell orientation is supported by published reports that showed that although astrocytes physiologically express large amounts of GFAP, Müller cells physiologically do not express GFAP or contain negligible amounts [39,40]. However, during periods of retinal stress or disease, such as retinal degeneration, oxidative stress, or diabetic retinopathy, numerous studies have shown that Müller cells are genetically altered and express GFAP [34,40,41], as in the present study.

In a murine model of diabetic retinopathy, the increase in GFAP expression has been shown to be a result of transcriptional activation of the GFAP gene in Müller cells [41].

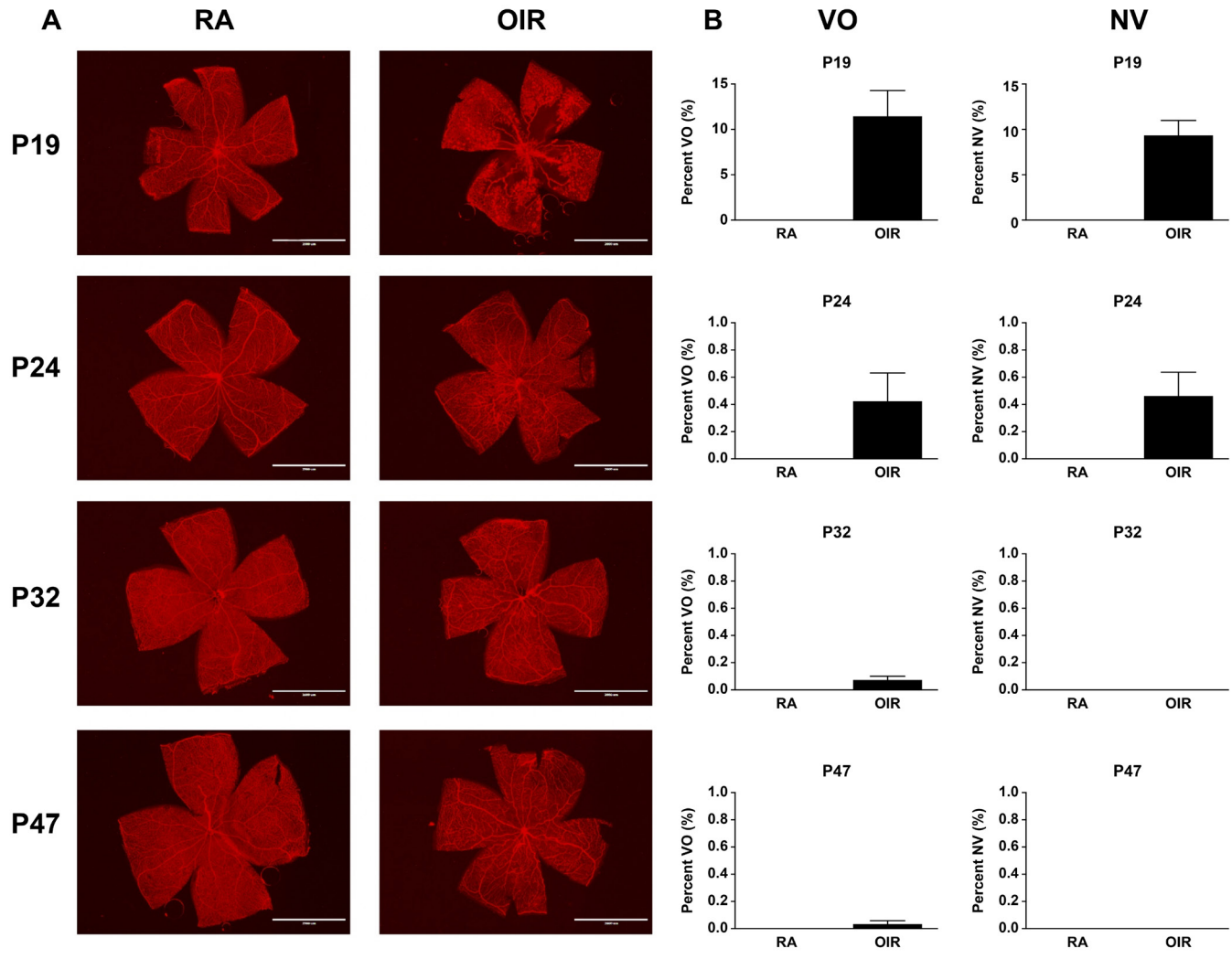

Figure 8. Assessment of retinal wholemount vaso-obliteration and neovascularization. **A**: Retinal wholemounts in RA mice (n = 4) and OIR mice (n = 4). The white arrow denotes activated microglia. **B**: Quantification of vaso-obliteration and neovascularization in retinal wholemounts. RA = room air; OIR = oxygen-induced ischemic retinopathy; P = postnatal day age; VO = vaso-obliteration; NV = neovascularization. At P19, four RA mice and four OIR mice were examined; at P24, three RA mice and four OIR mice; at P32, four RA mice and four OIR mice; and at P47, four RA mice and five OIR mice.

Alterations in GFAP expression are one of the earliest signs of retinal damage in OIR rats and correlate with the disease time course [34], as shown in the present study. Glia activation may underlie the increase in apoptotic loss of retinal neurons in the OIR mice and the disorganized cellular morphology seen in the present study. However, the cellular mechanisms regulating GFAP expression in Müller cells during OIR and the phenotypic and functional characterization of the Müller cells are unclear, and beyond the scope of this study.

Ectopic synapses were present throughout OIR recovery and corresponded to abnormal retinal function: Mal-aligned and ectopic neuronal synaptic connections between photoreceptor cells and second-order neurons were noted in the OIR mice throughout the time points tested in the present study (P19 to P47) in the central and peripheral retina. This is supported by similar findings of thinning of the OPL and loss of synaptic contact between the photoreceptor layer and the inner retina in OIR rats [42]. The quantification in the present study of the PKC-alpha stained bipolar cells and the PSD95 stained photoreceptor cells shows that in the central retina, the bipolar cells in the OIR mice were preserved, while the number of photoreceptor cells was lower; in the periphery, the number of bipolar cells and photoreceptor cells in the OIR mice was decreased. This structural abnormality of synapses is known to be correlated with functional impairment represented by loss or reduction of fERG b-waves [43-50]. The OIR mice, in the present study, showed a reduction in the b-wave amplitude at moderate and high flash intensities at P47 while the a-wave amplitude derived from photoreceptor responses in age-matched RA mice at the same flash intensities was relatively unaffected. These results indicate potential functional impairment of the synapses between photoreceptor cells and bipolar cells, loss or aberrant function of bipolar cells, or both.

Functional impairment may be in part related to structural damage or cell death in the inner and outer retina, as evidenced by the present findings of a decrease in the ONL thickness in the retinal cross sections in the OIR mice at P19 and P47 compared to the RA mice, a decrease in the INL in the OIR mice at P19 and P47, and increased apoptosis in the inner and outer retina of the OIR mice, predominantly in the ONL in the present study. Ectopic localization of photoreceptor synapses and retinal functional abnormalities have been observed in multiple mutant mouse lines [43-45,51]. Although abnormalities in presynaptic photoreceptor molecules have been associated with the appearance of ectopic synapses [42-45,48,49], the exact cellular and molecular mechanisms involved in the formation of ectopic synapses, as well as the complexities of pre- and postsynaptic interactions between rod and cone bipolar cells, and their corresponding photoreceptor cells are still to be determined, but are beyond the scope of this study.

In conclusion, this study expanded the ROP phenotypes in OIR mice, including prolonged glial cell activation, ectopic synapses, and apoptosis, beyond the relatively young ages at which these phenotypes had been previously characterized. The present study results suggest that the effects of hyperoxia during the neonatal period persist even after the whole retina, including the periphery, is vascularized in the adult stage. Considering these long-term effects of hyperoxia on retinal structure and function, molecular intervention in early phases of ROP would be essential. Further studies of mechanistic signaling pathways regulating cross talk between retinal glia, neurons, and vascular cells will identify potential cellular therapeutic targets to prevent adverse visual outcomes especially in patients with treated or regressed ROP at older age.

ACKNOWLEDGMENTS

The authors thank Dr. Ellen Wald (Department of Pediatrics, University of Wisconsin, Madison) for review of the manuscript. The authors also thank Satoshi Kinoshita for generation of frozen sections. The work in OJM laboratory is supported by the Department of Pediatrics and School of Graduate Studies, University of Wisconsin, Madison. The work in AI laboratory is supported by National Institutes of Health (R01EY022086) and Timothy William Trout Professorship in Eye Research. ELM is supported by the NIH predoctoral training program in Genetics (T32GM007133). The work in NS laboratory is supported by an unrestricted award from Research to Prevent Blindness to the Department of Ophthalmology and Visual Sciences, Retina Research Foundation (P30EY016665, P30CA014520, and R01EY026078). NS is a recipient of RPB Stein Innovation Award. Meeting Presentation: This research was presented in part at the Experimental Biology Meeting, April 21st 2018, in San Diego, CA.

REFERENCES

1. Smith LE, Shen W, Perruzzi C, Soker S, Kinose F, Xu X, Robinson G, Driver S, Bischoff J, Zhang B, Schaeffer JM, Senger DR. Regulation of vascular endothelial growth factor-dependent retinal neovascularization by insulin-like growth factor-1 receptor. Nat Med 1999; 5:1390-5. [PMID: 10581081].

2. Smith LE. Pathogenesis of retinopathy of prematurity. Growth Horm IGF Res 2004; 14:S140-4. [PMID: 15135797].

3. Good WV. Final results of the Early Treatment for Retinopathy of Prematurity (ETROP) randomized trial. Trans Am Ophthalmol Soc 2004; 102:233-48. , discussion 48–50.. [PMID: 15747762].
4. Mintz-Hittner HA, Kennedy KA, Chuang AZ. Efficacy of Intravitreal Bevacizumab for Stage 3+ Retinopathy of Prematurity. N Engl J Med 2011; 364:603-15. [PMID: 21323540].
5. Gilbert C. Retinopathy of prematurity: A global perspective of the epidemics, population of babies at risk and implications for control. Early Hum Dev 2008; 84:77-82. [PMID: 18234457].
6. Blencowe H, Moxon S, Gilbert C. Update on Blindness Due to Retinopathy of Prematurity Globally and in India. Indian Pediatr 2016; 53:Suppl 2S89-92. [PMID: 27915313].
7. Lee YS, Chang SHL, Wu SC, See LC, Chang SH, Yang ML, Wu WC. The inner retinal structures of the eyes of children with a history of retinopathy of prematurity. Eye (Lond) 2018; 32:104-12. [PMID: 28776594].
8. Yang CS, Wang AG, Sung CS, Hsu WM, Lee FL, Lee SM. Long-term visual outcomes of laser-treated threshold retinopathy of prematurity: a study of refractive status at 7 years. Eye (Lond) 2010; 24:14-20. [PMID: 19343053].
9. Hreinsdottir J, Fredriksson Kaul Y, Hellstrom-Westas L, Rosander K, von Hofsten C, Holmstrom G. Impaired cognitive ability at 2.5 years predicts later visual and ophthalmological problems in children born very preterm. Acta Paediatr 2018; 107:822-30. [PMID: 29288532].
10. O'Connor AR, Stephenson T, Johnson A, Tobin MJ, Moseley MJ, Ratib S, Ng Y, Fielder AR. Long-Term Ophthalmic Outcome of Low Birth Weight Children With and Without Retinopathy of Prematurity. Pediatrics 2002; 109:12-8. [PMID: 11773536].
11. Bringmann A, Pannicke T, Grosche J, Francke M, Wiedemann P, Skatchkov SN, Osborne NN, Reichenbach A. Muller cells in the healthy and diseased retina. Prog Retin Eye Res 2006; 25:397-424. [PMID: 16839797].
12. Zhang Y, Stone J. Role of astrocytes in the control of developing retinal vessels. Invest Ophthalmol Vis Sci 1997; 38:1653-66. [PMID: 9286254].
13. Davalos D, Grutzendler J, Yang G, Kim JV, Zuo Y, Jung S, Littman DR, Dustin ML, Gan WB. ATP mediates rapid microglial response to local brain injury in vivo. Nat Neurosci 2005; 8:752-8. [PMID: 15895084].
14. Kreutzberg GW. Microglia: a sensor for pathological events in the CNS. Trends Neurosci 1996; 19:312-8. [PMID: 8843599].
15. Fischer F, Martin G, Agostini HT. Activation of retinal microglia rather than microglial cell density correlates with retinal neovascularization in the mouse model of oxygen-induced retinopathy. J Neuroinflammation 2011; 8:120-[PMID: 21943408].
16. Vessey KA, Wilkinson-Berka J, Fletcher E. Characterization of retinal function and glial cell response in a mouse model of oxygen-induced retinopathy. J Comp Neurol 2011; 519:506-27. [PMID: 21192081].
17. Xu W, Hu Z, Lv Y, Dou G, Zhang Z, Wang H, Wang Y. Microglial density determines the appearance of pathological neovascular tufts in oxygen-induced retinopathy. Cell Tissue Res 2018; 374:25-38. [PMID: 29767277].
18. Smith LE, Wesolowski E, McLellan A, Kostyk SK, D'Amato R, Sullivan R, D'Amore PA. Oxygen-induced retinopathy in the mouse. Invest Ophthalmol Vis Sci 1994; 35:101-11. [PMID: 7507904].
19. Penn JS, Henry MM, Tolman BL. Exposure to alternating hypoxia and hyperoxia causes severe proliferative retinopathy in the newborn rat. Pediatr Res 1994; 36:724-31. [PMID: 7898981].
20. Dorfman AL, Dembinska O, Chemtob S, Lachapelle P. Structural and functional consequences of trolox C treatment in the rat model of postnatal hyperoxia. Invest Ophthalmol Vis Sci 2006; 47:1101-8. [PMID: 16505047].
21. Mezu-Ndubuisi OJ, Adams T, Taylor LK, Nwaba A, Eickhoff J. Simultaneous assessment of aberrant retinal vascularization, thickness, and function in an in vivo mouse oxygen-induced retinopathy model. Eye (Lond) 2019; 33:363-373. [PMID: 30209267].
22. Mezu-Ndubuisi OJ. In Vivo Angiography Quantifies Oxygen-Induced Retinopathy Vascular Recovery. Optom Vis Sci 2016; 93:1268-[PMID: 27668493].
23. Mezu-Ndubuisi OJ, Taylor LK, Schoephoerster JA. Simultaneous Fluorescein Angiography and Spectral Domain Optical Coherence Tomography correlate Retinal Thickness Changes to Vascular Abnormalities in an In vivo Mouse Model of Retinopathy of Prematurity. J Ophthalmol 2017; 9620876[PMID: 28573047].
24. Vidal L, Diaz F, Villena A, Moreno M, Campos JG, Perez de Vargas I. Reaction of Muller cells in an experimental rat model of increased intraocular pressure following timolol, latanoprost and brimonidine. Brain Res Bull 2010; 82:18-24. [PMID: 20206241].
25. Jonas RA, Yuan TF, Liang YX, Jonas JB, Tay DK, Ellis-Behnke RG. The spider effect: morphological and orienting classification of microglia in response to stimuli in vivo. PLoS One 2012; 7:e30763-[PMID: 22363486].
26. Mezu-Ndubuisi OJ, Wang Y, Schoephoerster J, Falero-Perez J, Zaitoun IS, Sheibani N, Gong S. Intravitreal Delivery of VEGF-A165-loaded PLGA Microparticles Reduces Retinal Vaso-Obliteration in an In Vivo Mouse Model of Retinopathy of Prematurity. Curr Eye Res 2019; 44:275-286. [PMID: 30383455].
27. Stahl A, Connor KM, Sapieha P, Willett KL, Krah NM, Dennison RJ, Chen J, Guerin KI, Smith LEH. Computer-aided quantification of retinal neovascularization. Angiogenesis 2009; 12:297-301. [PMID: 19757106].
28. Mezu-Ndubuisi OJ, Wanek J, Chau FY, Teng PY, Blair NP, Reddy NM, Raj JU, Reddy SP, Shahidi M. Correspondence of retinal thinning and vasculopathy in mice with oxygen-induced retinopathy. Exp Eye Res 2014; 122:119-22. [PMID: 24703909].

29. Higuchi H, Macke EL, Lee W-H, Miller SA, Xu JC, Ikeda S, Ikeda A. Genetic basis of age-dependent synaptic abnormalities in the retina. Mamm Genome 2015; 26:21-32. [PMID: 25273269].

30. Luna G, Keeley PW, Reese BE, Linberg KA, Lewis GP, Fisher SK. Astrocyte structural reactivity and plasticity in models of retinal detachment. Exp Eye Res 2016; 150:4-21. [PMID: 27060374].

31. McVicar CM, Hamilton R, Colhoun LM, Gardiner TA, Brines M, Cerami A, Stitt AW. Intervention with an erythropoietin-derived peptide protects against neuroglial and vascular degeneration during diabetic retinopathy. Diabetes 2011; 60:2995-3005. [PMID: 21911748].

32. Wang W, Li Z, Sato T, Oshima Y. Tenomodulin inhibits retinal neovascularization in a mouse model of oxygen-induced retinopathy. Int J Mol Sci 2012; 13:15373-86. [PMID: 23203131].

33. Fielder A, Blencowe H, O'Connor A, Gilbert C. Impact of retinopathy of prematurity on ocular structures and visual functions. Arch Dis Child Fetal Neonatal Ed 2015; •••:F179-84. [PMID: 25336678].

34. Downie LE, Pianta MJ, Vingrys AJ, Wilkinson-Berka JL, Fletcher EL. Neuronal and glial cell changes are determined by retinal vascularization in retinopathy of prematurity. J Comp Neurol 2007; 504:404-17. [PMID: 17663451].

35. Gu X, Samuel S, El-Shabrawey M, Caldwell RB, Bartoli M, Marcus DM, Brooks SE. Effects of sustained hyperoxia on revascularization in experimental retinopathy of prematurity. Invest Ophthalmol Vis Sci 2002; 43:496-502. [PMID: 11818396].

36. Stone J, Itin A, Alon T, Pe'er J, Gnessin H, Chan-Ling T, Keshet E. Development of retinal vasculature is mediated by hypoxia-induced vascular endothelial growth factor (VEGF) expression by neuroglia. J Neurosci 1995; 15:4738-47. [PMID: 7623107].

37. Eichler W, Yafai Y, Keller T, Wiedemann P, Reichenbach A. PEDF derived from glial Müller cells: a possible regulator of retinal angiogenesis. Exp Cell Res 2004; 299:68-78. [PMID: 15302574].

38. Kaur C, Sivakumar V, Foulds WS, Luu CD, Ling EA. Cellular and vascular changes in the retina of neonatal rats after an acute exposure to hypoxia. Invest Ophthalmol Vis Sci 2009; 50:5364-74. [PMID: 19474404].

39. Eng LF, Dearmond SJ. Immunocytochemical studies of astrocytes in normal development and disease. Advances in cellular neurobiology. 3: Elsevier; 1982. p. 145–71.

40. Ekström P, Sanyal S, Narfström K, Chader G, van Veen T. Accumulation of glial fibrillary acidic protein in Müller radial glia during retinal degeneration. Invest Ophthalmol Vis Sci 1988; 29:1363-71. [PMID: 3417421].

41. Tabasi A, Ghafari S, Mehdizadeh M, Shekari MA, Golalipour MJ. Gestational diabetes influences retinal Muller cells in rat's offspring. Iran J Basic Med Sci 2017; 20:216-[PMID: 28293400].

42. Dorfman AL, Cuenca N, Pinilla I, Chemtob S, Lachapelle P. Immunohistochemical evidence of synaptic retraction, cytoarchitectural remodeling, and cell death in the inner retina of the rat model of oygen-induced retinopathy (OIR). Invest Ophthalmol Vis Sci 2011; 52:1693-708. [PMID: 21071736].

43. Johnson BA, Ikeda S, Pinto LH, Ikeda A. Reduced synaptic vesicle density and aberrant synaptic localization caused by a splice site mutation in the Rs1h gene. Vis Neurosci 2006; 23:887-98. [PMID: 17266781].

44. Mansergh F, Orton NC, Vessey JP, Lalonde MR, Stell WK, Tremblay F, Barnes S, Rancourt DE, Bech-Hansen NT. Mutation of the calcium channel gene Cacna1f disrupts calcium signaling, synaptic transmission and cellular organization in mouse retina. Hum Mol Genet 2005; 14:3035-46. [PMID: 16155113].

45. Dick O, tom Dieck S, Altrock WD, Ammermuller J, Weiler R, Garner CC, Gundelfinger ED, Brandstatter JH. The presynaptic active zone protein bassoon is essential for photoreceptor ribbon synapse formation in the retina. Neuron 2003; 37:775-86. [PMID: 12628168].

46. Ou J, Vijayasarathy C, Ziccardi L, Chen S, Zeng Y, Marangoni D, Pope JG, Bush RA, Wu Z, Li W, Sieving PA. Synaptic pathology and therapeutic repair in adult retinoschisis mouse by AAV-RS1 transfer. J Clin Invest 2015; 125:2891-903. [PMID: 26098217].

47. Takada Y, Vijayasarathy C, Zeng Y, Kjellstrom S, Bush RA, Sieving PA. Synaptic pathology in retinoschisis knockout (Rs1-/y) mouse retina and modification by rAAV-Rs1 gene delivery. Invest Ophthalmol Vis Sci 2008; 49:3677-86. [PMID: 18660429].

48. Chang B, Heckenlively JR, Bayley PR, Brecha NC, Davisson MT, Hawes NL, Hirano AA, Hurd RE, Ikeda A, Johnson BA, McCall MA, Morgans CW, Nusinowitz S, Peachey NS, Rice DS, Vessey KA, Gregg RG. The nob2 mouse, a null mutation in Cacna1f: anatomical and functional abnormalities in the outer retina and their consequences on ganglion cell visual responses. Vis Neurosci 2006; 23:11-24. [PMID: 16597347].

49. Haeseleer F, Imanishi Y, Maeda T, Possin DE, Maeda A, Lee A, Rieke F, Palczewski K. Essential role of Ca2+-binding protein 4, a Cav1.4 channel regulator, in photoreceptor synaptic function. Nat Neurosci 2004; 7:1079-87. [PMID: 15452577].

50. Caicedo A, Espinosa-Heidmann DG, Hamasaki D, Pina Y, Cousins SW. Photoreceptor synapses degenerate early in experimental choroidal neovascularization. J Comp Neurol 2005; 483:263-77. [PMID: 15682400].

51. Lee WH, Higuchi H, Ikeda S, Macke EL, Takimoto T, Pattnaik BR, Liu C, Chu LF, Siepka SM, Krentz KJ, Rubinstein CD, Kalejta RF, Thomson JA, Mullins RF, Takahashi JS, Pinto LH, Ikeda A. Mouse Tmem135 mutation reveals a mechanism involving mitochondrial dynamics that leads to age-dependent retinal pathologies. eLife 2016; •••:5-[PMID: 27863209].

Articles are provided courtesy of Emory University and the Zhongshan Ophthalmic Center, Sun Yat-sen University, P.R. China. The print version of this article was created on 1 April 2020. This reflects all typographical corrections and errata to the article through that date. Details of any changes may be found in the online version of the article.